Aalto University

This is an electronic reprint of the original article.
This reprint may differ from the original in pagination and typographic detail.

Hassa, A.; Von Wenckstern, H.; Splith, D.; Sturm, C.; Kneiß, M.; Prozheeva, V.; Grundmann, M.

Structural, optical, and electrical properties of orthorhombic κ-$(In_xGa_{1-x})_2O_3$ thin films

Published in:
APL Materials

DOI:
10.1063/1.5054394

Published: 01/02/2019

Document Version
Publisher's PDF, also known as Version of record

Published under the following license:
CC BY

Please cite the original version:
Hassa, A., Von Wenckstern, H., Splith, D., Sturm, C., Kneiß, M., Prozheeva, V., & Grundmann, M. (2019). Structural, optical, and electrical properties of orthorhombic -$(In_xGa_{1-x})_2O_3$ thin films. *APL Materials*, *7*(2), 1-9. [022525]. https://doi.org/10.1063/1.5054394

This material is protected by copyright and other intellectual property rights, and duplication or sale of all or part of any of the repository collections is not permitted, except that material may be duplicated by you for your research use or educational purposes in electronic or print form. You must obtain permission for any other use. Electronic or print copies may not be offered, whether for sale or otherwise to anyone who is not an authorised user.

APL Materials

Structural, optical, and electrical properties of orthorhombic κ-$(In_xGa_{1-x})_2O_3$ thin films

Cite as: APL Mater. **7**, 022525 (2019); https://doi.org/10.1063/1.5054394
Submitted: 31 August 2018 . Accepted: 19 December 2018 . Published Online: 06 February 2019

A. Hassa, H. von Wenckstern, D. Splith, C. Sturm, M. Kneiß, V. Prozheeva, and M. Grundmann

ARTICLES YOU MAY BE INTERESTED IN

Tin-assisted heteroepitaxial PLD-growth of κ-Ga_2O_3 thin films with high crystalline quality
APL Materials **7**, 022516 (2019); https://doi.org/10.1063/1.5054378

The electronic structure of ε-Ga_2O_3
APL Materials **7**, 022522 (2019); https://doi.org/10.1063/1.5054395

Deep acceptors and their diffusion in Ga_2O_3
APL Materials **7**, 022519 (2019); https://doi.org/10.1063/1.5063807

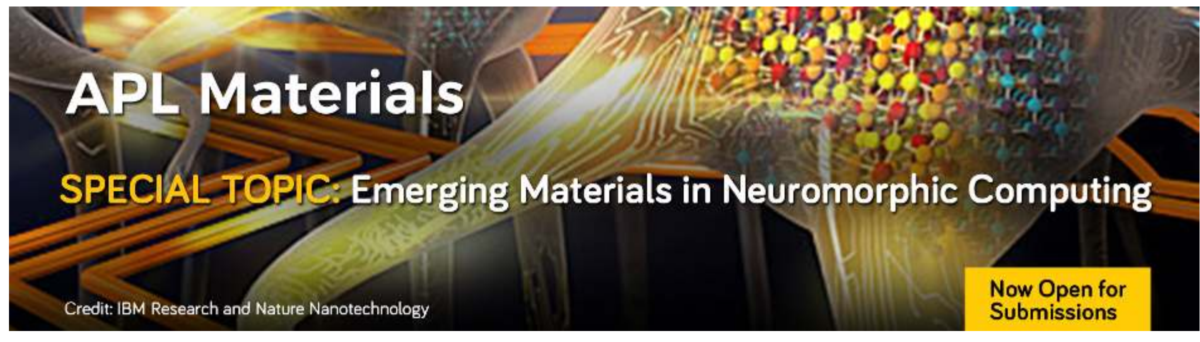

© 2019 Author(s).

Structural, optical, and electrical properties of orthorhombic κ-$(In_xGa_{1-x})_2O_3$ thin films

Cite as: APL Mater. **7**, 022525 (2019); doi: 10.1063/1.5054394
Submitted: 31 August 2018 • Accepted: 19 December 2018 •
Published Online: 6 February 2019

View Online Export Citation CrossMark

A. Hassa,[1] H. von Wenckstern,[1] D. Splith,[1] C. Sturm,[1] M. Kneiß,[1] V. Prozheeva,[2] and M. Grundmann[1]

AFFILIATIONS

[1]Felix Bloch Institute for Solid State Physics, Universität Leipzig, Linnéstraße 5, 04103 Leipzig, Germany
[2]Department of Applied Physics, Aalto University, P.O. Box 15100, FIN-00076 Aalto, Finland

ABSTRACT

Material properties of orthorhombic κ-phase $(In_xGa_{1-x})_2O_3$ thin films grown on a c-plane sapphire substrate by pulsed-laser deposition are reported for an indium content up to $x \sim 0.35$. This extended range of miscibility enables band gap engineering between 4.3 and 4.9 eV. The c-lattice constant as well as the bandgap depends linearly on the In content. For $x > 0.35$, a phase change to the hexagonal $InGaO_3$(II) and the cubic bixbyite structure occurred. The dielectric function and the refractive index were determined by spectroscopic ellipsometry as a function of the alloy composition. We propose zirconium to induce n-type conductivity and have achieved electrically conducting thin films with a room temperature conductivity of up to 0.1 S/cm for samples with a low In content of about $x = 0.01$. Temperature-dependent Hall-effect measurements yielded a thermal activation energy of the free electron density of 190 meV. Schottky barrier diodes with rectification ratios up to 10^6 were investigated by quasi-static capacitance voltage and temperature-dependent current voltage measurements.

© 2019 Author(s). *All article content, except where otherwise noted, is licensed under a Creative Commons Attribution* (CC BY) *license* (*http://creativecommons.org/licenses/by/4.0/*). https://doi.org/10.1063/1.5054394

Wide band gap semiconducting oxides such as ZnO and SnO_2 or the group-III sesquioxides In_2O_3 and Ga_2O_3 find potential application as photo detectors,[1] gas sensors,[2] thin film transistors[3] and in high-power electronics.[4–7] Research on Ga_2O_3 and its alloys has increased tremendously after the demonstration of a metal-semiconductor field-effect transistor using a Ga_2O_3 layer grown homoepitaxially by molecular beam epitaxy.[8] Ga_2O_3 single crystals are available for the thermodynamically most stable polymorph (beta-gallia structure) having a monoclinic lattice symmetry, and hence, the majority of Ga_2O_3-related publications deal with β-Ga_2O_3. Rhombohedral α-Ga_2O_3 is of interest and investigated as well since it has the same lattice structure as thermodynamically stable α-Al_2O_3 and metastable α-In_2O_3 and would allow band gap engineering in a wide composition range. Recent reviews summarize material properties and devices based on monoclinic and/or rhombohedral $(In,Ga,Al)_2O_3$.[5–7,9] Maccioni and Fiorentini predicted a large polarization of 23 $\mu C/cm^2$ for orthorhombic Ga_2O_3 which is similar to that of $BaTiO_3$ and about three times larger than that of AlN.[10] In 2018, Cho and Mishra[11] predicted an identical polarization for this modification and Kim *et al.*[12] calculated a value of 26.39 $\mu C/cm^2$. The crystal structure of orthorhombic Ga_2O_3 was described in detail by Cora *et al.*, and a much smaller polarization of 0.2 $\mu C/cm^2$ was deduced from the atomic coordinates[13] being in close agreement with the value of 0.18 $\mu C/cm^2$ obtained from dynamic hysteresis measurements.[14] The difference between the predicted and the experimentally determined values needs to be resolved to judge the true potential of orthorhombic Ga_2O_3 for high electron mobility transistors for which band gap engineering is required as well. Binary thin films were obtained by halide vapor phase epitaxy,[15] metal-organic chemical vapor deposition,[13,14,16–18] atomic layer deposition,[17] and tin-assisted growth by pulsed-laser deposition (PLD)[19] or molecular beam epitaxy.[20] In the latter samples, tin does not contribute free electrons at room temperature (RT).[19] So far, successful n-type doping was not reported. In nominally undoped samples, electrical conductivity was observed for $T > 400$ K with a thermal activation energy of 695 meV.[21] Furthermore, such samples were used to fabricate a photo conductive UV-detector. Ternary layers were obtained on a c-plane sapphire substrate [with an AlN

© Author(s) 2019

buffer layer for $(Al,Ga)_2O_3$] by mist chemical vapor deposition.[22,23] For $(In_xGa_{1-x})_2O_3$, phase separation was reported for $x > 0.2$ (cubic phase formed).[23] The optical bandgap decreased from 5 eV for $x = 0$ to 4.5 eV for $x = 0.2$. The indium incorporation leads to an increase in the c-lattice constant that can be described by $c(x) = (0.9274 + 0.1075 \cdot x)$ nm.

We have achieved n-conducting κ-phase $(In_{0.01}Ga_{0.99})_2O_3$:Zr thin films with a free electron concentration of $n = 2 \times 10^{16}$ cm^{-3} at RT. The conductivity of such samples was sufficient to achieve Schottky barrier diodes with rectification ratios up to 10^6. Further, we stabilized $(In_xGa_{1-x})_2O_3$ thin films in the κ-phase polymorph up to $x \sim 0.35$ and report structural, morphological, and optical properties as a function of the alloy composition.

$(In_xGa_{1-x})_2O_3$ thin films were grown by pulsed-laser deposition (PLD) at a temperature of 940 K and an oxygen partial pressure of 3×10^{-4} mbar. The c-sapphire substrates were either 2 inch in diameter or 10×10 mm^2 sized quadratic pieces. For investigations of material properties in dependence on the indium content, we used a thin film with laterally continuous composition spread (CCS) that was deposited from a ceramic target consisting of two semi-circular segments. One segment consists of Ga_2O_3 (purity 99.999%, Alfa Aeser) and the other of In_2O_3 (purity 99.994%, Alfa Aeser). Both segments have an admixture of 2.5 wt. % SnO_2 (purity 99.999%, Alfa Aeser), which equals approximately 1.6 at. % in Ga_2O_3 and 2.3 at. % in In_2O_3, to induce the growth of κ-phase thin films as described by Orita *et al.*[19] and by Kracht *et al.*[20] Details about our CCS-PLD approach can be found in Ref. 24. To enhance the n-type conductivity of κ-$(In_{0.01}Ga_{0.99})_2O_3$, zirconium was used as a doping element, resulting in a concentration of approximately 1.3 at. % in the thin film.

The PLD setup consists of a KrF excimer laser (248 nm) focused to an energy density of 2 J cm^{-2} at the target. The distance between the target and the substrate was 10 cm. The composition of the thin films was determined by energy-dispersive X-ray spectroscopy (EDX) using a FEI Nova Nanolab 200 equipped with an Ametek EDAX detector. X-ray diffraction (XRD) measurements were performed with a PANalytical X'pert PRO MRD diffractometer equipped with a PIXcel^{3D} detector operating in a 1D scanning line mode with 255 channels. The surface morphology was determined with a Park Systems XE-150 atomic force microscope in a non-contact mode. The optical properties were investigated by spectroscopic ellipsometry using a J. A. Woollam dual rotating compensator ellipsometer RC2. Electrical properties were investigated by using current-voltage measurements of ohmic and Schottky barrier contacts, which were realized using recipes optimized for monoclinic Ga_2O_3. The ohmic contacts consist of a thermally evaporated layer stack of Ti/Al/Au and were annealed subsequently at 773 K for 10 min in nitrogen ambient.[25] For the Schottky barrier contacts, Pt was reactively sputtered[26] in a peripheral position (off-axis configuration),[27] and finally, a Pt layer was sputtered in an inert Ar ambient to assure current spreading.[26,27]

Temperature-dependent resistivity and Hall-effect measurements were performed for $T \leq 350$ K inside a Quantum Design physical property measurement system (PPMS) at a magnetic field of 1 T using a Keithley current source, switch system, and multimeter. Temperature-dependent resistivity and Hall-effect measurements for $T \geq 350$ K were performed inside a home-built high temperature thermostat at a magnetic field of 0.43 T using a Keithley current source, switch system, and multimeter and a Lakeshore 331 temperature controller.

Current-voltage (IV) measurements and quasi-static capacitance-voltage (CV) measurements on Schottky-contacts (SCs) were performed in a Süss Waferprober System P200 connected to an Agilent 4155C Semiconductor Parameter Analyzer. For temperature-dependent measurement between 100 and 320 K, a piece of one of the samples was mounted on a TO18 socket and a diode was contacted using gold wire and silver epoxy resin. The measurement was performed inside a cryostat using again the Agilent 4155C Semiconductor Parameter Analyzer. For the temperature-dependent measurement between 300 and 700 K, the same piece was removed from the socket and put inside a Linkam HFS600E-PB4 Probe Stage.

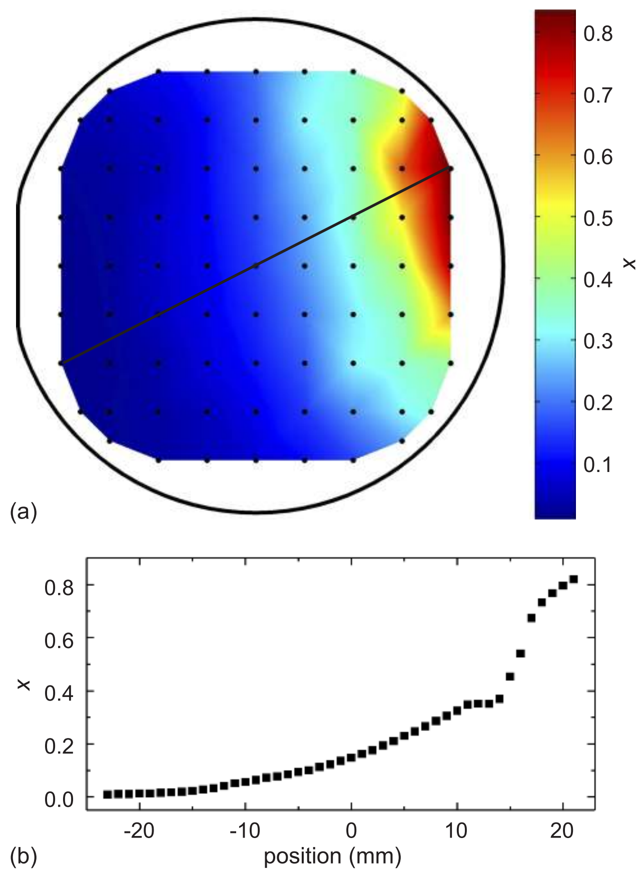

FIG. 1. (a) False color representation of the In content x of a $(In_xGa_{1-x})_2O_3$ thin film grown on a 2 inch diameter c-plane sapphire substrate. The black dots indicate measurement spots, data in between was interpolated. (b) shows the EDX-linescan along the compositional gradient as indicated by the black line in (a).

© Author(s) 2019

Inside the stage, the diode was contacted with tungsten probe needles. An Agilent 4156C Semiconductor Parameter Analyzer was used for this measurement. The temperature was calculated from a reference measurement of a Pt100 resistor inside the probe stage.

The lateral variation of the cation composition of the CCS-PLD thin film was determined by EDX measurements and is depicted in Fig. 1(a). It exhibits a non-linear increase in the indium content x along the gradient direction as visible in Fig. 1(b). The strong increase in the gradient, observed for positions $z > 15$ mm, is connected to phase separation as concluded from 55 2θ-ω measurements recorded with a step size of 1 mm along the gradient direction. The results are represented as a false color map in Fig. 2(a). For $x = 0.1$, a single XRD 2θ-ω scan is shown in Fig. 2(c). Around $x \sim 0.35$ (corresponding to the position $z = 15$ mm) and $x \sim 0.5$, changes of the predominant crystallographic phase are evident. In the region of $0.35 < x < 0.5$, the hexagonal $InGaO_3$(II) phase appears, and for higher In concentrations ($x > 0.5$), the cubic bixbyite structure is found. For $x \le 0.35$, a series of narrow peaks, shifting to lower angles with increasing In content, are observed. The peak positions occur for each In content systematically at higher angles compared to those of monoclinic $(In_xGa_{1-x})_2O_3$ thin films[28–30] indicating growth in the orthorhombic modification. To clarify this assumption, XRD ϕ-scans were recorded for five selected In contents for asymmetric reflections corresponding to the (131), (122), and (206) lattice planes of the κ-phase shown in Fig. 2(b) for $x = 0.01$. The 2θ and χ positions of these reflections were assumed to be the same as for binary κ-Ga_2O_3 based on the unit cell by Cora *et al.*[13] due to a lack of data on composition-dependent lattice constants for the alloy. Both the (131) and (206) reflections occur six-fold with a separation of 60° indicating epitaxial growth on the c-sapphire substrate. Assuming an orthorhombic unit cell, this six-fold symmetry suggests three rotational domains separated by 120°.[31] The orthorhombic symmetry of the unit cell was confirmed by the twelve-fold occurring (122) reflection, where an additional two-fold splitting of the peaks is due to mirror planes in the orthorhombic structure. Furthermore, according to calculations using the VESTA software package,[32] there should be no reflection observable for this specific set of angles in the hexagonal equivalent of this phase, typically referred to as ε-Ga_2O_3[33] instead of κ-Ga_2O_3. These results unambiguously substantiate the growth in orthorhombic modification for $x \le 0.35$.

The epitaxial relationship deduced from the positions of the film reflections in the XRD ϕ-scans with respect to those of the α-Al_2O_3 (10.2) plane are κ-$(In_xGa_{1-x})_2O_3$ $\langle 010\rangle \| \alpha$-$Al_2O_3$ $\langle 10\bar{1}0\rangle$ and κ-$(In_xGa_{1-x})_2O_3$ $\langle 100\rangle \| \alpha$-$Al_2O_3$ $\langle 2\bar{1}\bar{1}0\rangle$. With that, the peaks in Fig. 2(a) for $x \le 0.35$ can be assigned to the $(00n)$ reflections of orthorhombic $(In_xGa_{1-x})_2O_3$. Hence, we extended the composition range for which κ-phase thin films were reported; samples grown by mist-CVD showed phase separation for $x > 0.2$.[23]

The dependence of the c-lattice constant on the indium content is shown in Fig. 4. It increases linearly with x and can be modeled in close agreement with the data of Nishinaka *et al.*[23] by $c = [(9.269 \pm 0.004) + (1.097 \pm 0.01) \cdot x\,]$ Å. For a lower indium content, a non-linearity in $c(x)$ is observed that we attribute to slightly different sample alignment between the chemical and the structural analysis.

The growth rate τ was calculated from the sample thickness (deduced from spectroscopic ellipsometry, see below) and starts for the lowest In content at $\tau = 8.7$ pm/pulse and saturates around 7.2 pm/pulse for $x \ge 0.2$. For monoclinic $(In_xGa_{1-x})_2O_3$, the growth rate is only 2 pm/pulse for the lowest In content and saturated at 4 pm/pulse for $x > 0.05$[30] for similar deposition conditions. Since the incident particle flux on the substrate is, except for tin, the same for the CCS-PLD growth of monoclinic $(In_xGa_{1-x})_2O_3$ and orthorhombic

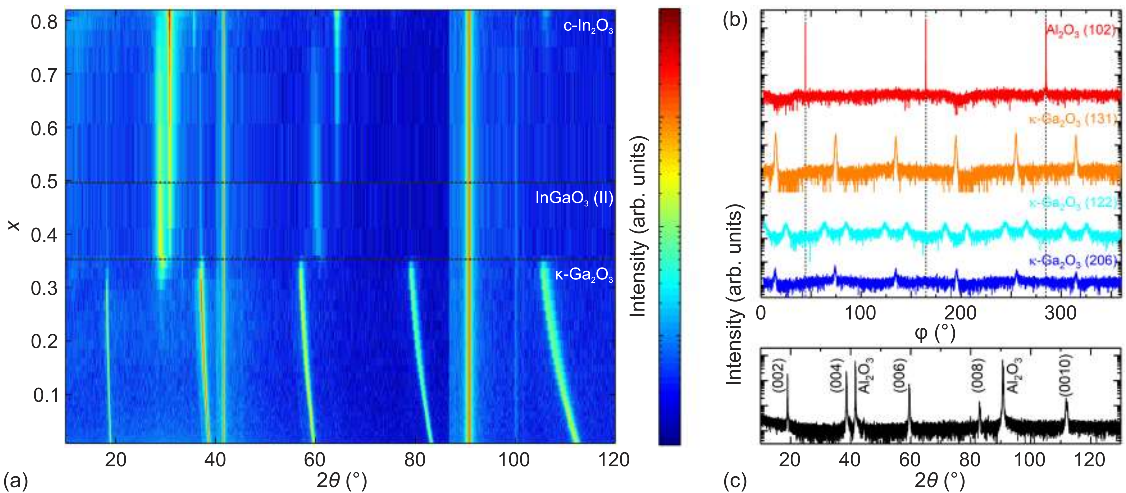

FIG. 2. (a) False color plot of 55 XRD 2θ-ω measurements acquired along a gradient direction. (b) XRD ϕ-scans and (c) single XRD 2θ-ω measurement of a sample piece at $x \sim 0.01$.

© Author(s) 2019

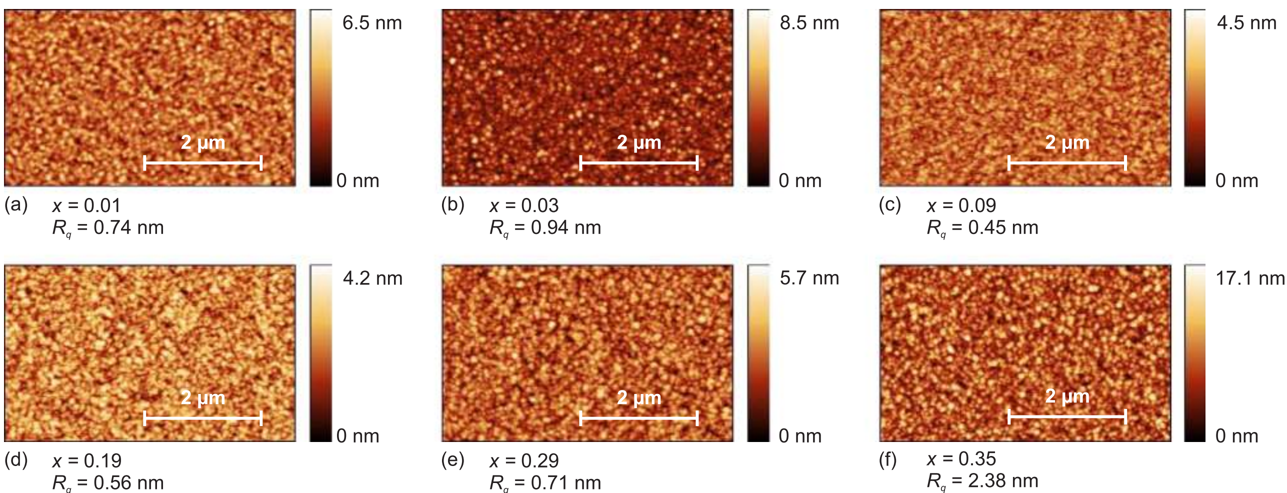

FIG. 3. Surface morphology and corresponding surface roughness R_q measured by atomic force microscopy for In contents x as labeled.

$(In_xGa_{1-x})_2O_3$:Sn, the increased growth rate for the κ-phase is assigned to a strong reduction of the desorption of volatile Ga_2O. This is in line with findings of Kracht *et al.*[20] who proposed an oxidation of gallium suboxides by reducing SnO or SnO_2 at the surface, which leads to an increased incorporation of gallium and with that to higher growth rates compared to tin-free growth. That the presence of tin is beneficial for the stabilization of PLD thin films with an orthorhombic phase was already pointed out in 2002 by Orita *et al.*[19] who investigated tin-doped Ga_2O_3 as a possible transparent conducting oxide (TCO) material. Further, they demonstrated that tin is not contributing to the electrical conductivity at RT likely due to tin-related donor states being too deep to generate free electrons at RT. EDX measurements on our CCS-PLD thin films indicate the presence of about 0.6–0.8 at. % tin in orthorhombic $(In_xGa_{1-x})_2O_3$, however, an electrical conductivity was not measurable corroborating results of Orita *et al.* that tin is not donating free electrons in orthorhombic $(In_xGa_{1-x})_2O_3$:Sn at RT.

The surface morphology was investigated by AFM measurements to deduce the root mean square surface roughness R_q. Figure 3 depicts images of the thin film surfaces of the orthorhombic part for six different In contents. The images show smooth surfaces for $x < 0.35$ with low R_q values ranging between 0.45 nm and 0.94 nm independent of x. For the highest In content in orthorhombic modification, $x = 0.35$, an increased R_q of 2.38 nm caused by the phase transition from orthorhombic into hexagonal $InGaO_3$(II) phase was observed. The grains are spherically shaped with diameters of approximately 100–120 nm for all In contents.

The compositional dependence of the bandgap (Fig. 4) was determined by spectroscopic ellipsometry and shows three regimes with small differences in the slope. In general, the bandgap decreases as expected with increasing In content and allows band gap engineering between about 4.9 eV and 4.3 eV for $0 \leq x \leq 0.35$.

With spectroscopic ellipsometry measurements, the dielectric function (DF) was investigated in the spectral range between 0.74 eV and 6.3 eV for angles of incidence of 50°, 60°, and 70°. In order to reduce the impact of the composition gradient on an individual measurement, the spot size was reduced to about 300 × 500 μm^2 by using focusing optics.

Due to the presence of rotation domains, the optically biaxial films can be described by an uniaxial model with an optical axis parallel to the surface normal. Therefore, standard ellipsometry can be applied,[34] i.e., the ellipsometric parameters Ψ and Δ are given by

$$\rho = \frac{r_p}{r_s} = \tan \Psi e^{i\Delta}. \quad (1)$$

The abbreviations r_p and r_s represent the complex reflection coefficients for light polarized parallel and perpendicular

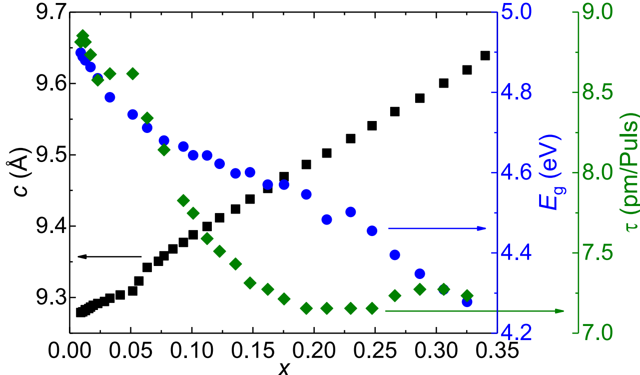

FIG. 4. The c-lattice constant determined from XRD patterns as well as the bandgap and growth rate obtained from spectroscopic ellipsometry measurements as a function of the In content x.

© Author(s) 2019

to the plane of incidence. To reduce the dependence of Ψ and Δ on the angle of incidence, it is appropriate to convert these quantities into a pseudodielectric function $\langle\epsilon\rangle$.[35] A layer stack model consisting of a c-plane sapphire substrate, a thin film, and a surface layer was used to obtain the dielectric function (DF). For the c-plane sapphire substrate, the optical constants were taken from Ref. 36. The thin film DF was described to be uniaxial, i.e., the DF tensor is given by $\epsilon_\perp = \epsilon_{xx} = \epsilon_{yy} \neq \epsilon_\parallel = \epsilon_{zz}$. In the analysis of the experimental data, it was found that the contribution of ϵ_{zz} cannot be neglected. The line shape of each tensor component was represented by model dielectric functions. Similar to former calculated DF of β-Ga_2O_3 thin films by Sturm *et al.*,[34] the excitonic contributions (χ^{exc}) were characterized by using a model function, which was developed by Tanguy.[37–39] For the weakly pronounced band-band transitions, which cannot be resolved separately, Gaussian oscillators (χ^{gauss}) were used. Due to the Kramers-Kronig transformation, the contributions of high-energy transitions to the real part of the DF were taken into account by a pole function (χ^{pole}). Since the optical axis is perpendicular to the surface, the sensitivity to $\epsilon_\parallel$ is quite low and the same transitions for $\epsilon_\perp$ and $\epsilon_\parallel$ can be assumed. Thus, the resulting DF is given by

$$\epsilon_i = \sum_{j=1}^{2} \chi_{j,i}^{\mathrm{exc}} + \chi_{j,i}^{\mathrm{gauss}} + \chi_j^{\mathrm{pole}}, \qquad (2)$$

with $i = \perp, \parallel$.

Because of the strong correlation between the parameters due to the absence of strong absorption features in the spectra, a further assumption for each transition is that they have the same energy and broadening in $\epsilon_\perp$ and $\epsilon_\parallel$. Finally, the surface roughness was described by an effective medium approach,[40] where the DF of the Ga_2O_3 thin film and air was mixed 1:1. The thickness of this layer was found to be about 2 nm. The experimentally recorded and calculated pseudodielectric functions are well coinciding as exemplary shown in Fig. 5 for selected In concentrations and an angle of incidence of 60°. For energies below 4 eV, the spectra are dominated by thickness oscillations allowing a precise determination of the film thickness, which is in the range of 180–205 nm. For energies larger than 4 eV, absorption sets in and the oscillations vanish such that the spectra are dominated by the excitonic and band-band transitions.

The deduced dielectric function is shown in Fig. 6 for selected In concentrations. As expected, a red shift of the onset of the absorption is observed with increasing In concentration caused by an almost linear red shift of the transition energies with respect to the In concentration. Besides the red shift of the transition energy, we also observe a strong increase in the excitonic broadening from 50 meV for $x \approx 0.01$ up to 350 meV for $x \approx 0.32$ due to alloy broadening. Interestingly, with increasing In concentrations, the difference of the line shape between $\epsilon_\perp$ and $\epsilon_\parallel$ decreases, which leads to a decrease in the optical anisotropy.

Besides the DF, another important quantity, especially for the design of applications, is the refractive index. In the transparent spectral range, the dispersion of the refractive index can be described by the Cauchy function, i.e., $n = A + B/\lambda^2 + C/\lambda$,[4] and the corresponding parameters are depicted in Fig. 2 in the supplementary material. The red shift of the transition energies leads to an increase in the refractive index expressed by an increase in the Cauchy parameters. However, for $x > 0.2$, a decrease in the Cauchy parameters A and C can be observed leading to a decrease in the refractive index especially at small energies. Up to now, the origin of this decrease is not fully understood, but the strong decrease, which is also observable in the real part of the DF as can be seen by the kink at $E \sim 1$ eV for $x = 0.3$, indicates the presence of free

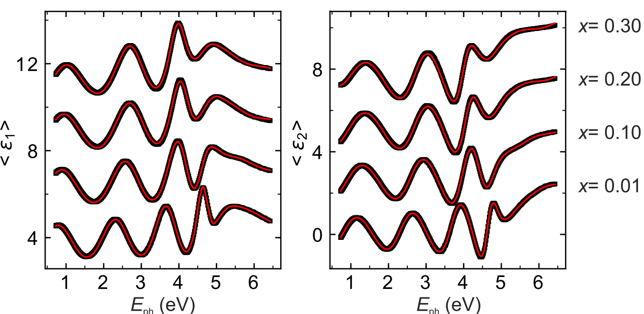

FIG. 5. The experimental (black squares) and calculated (red solid lines) pseudodielectric function for selected In concentration and an angle of incidence of 60°. For a better clarity, the spectra are shifted vertically.

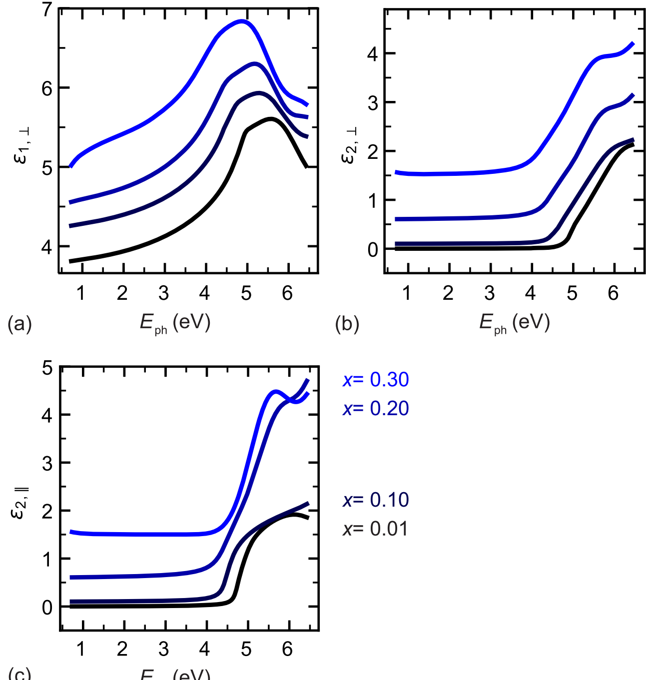

FIG. 6. Dielectric function (a) $\epsilon_{1,\perp}$, (b) $\epsilon_{2,\perp}$ and (c) $\epsilon_{2,\parallel}$ of κ-$(In_xGa_{1-x})_2O_3$ for indium contents as labeled.

© Author(s) 2019

charge carriers for these In concentrations, in contrast to Hall effect data. We assume that the transport of the carriers is suppressed due to the existence of potential barriers that cannot be passed at room temperature. The origin of such barriers is likely grain boundaries since rotational domains exist.

As stated above, tin does not contribute free electrons such that it is necessary to add an additional shallow donor in order to achieve n-type conductivity. As a suitable candidate in κ-modification, we identified zirconium and fabricated samples with a low In-content of $x \approx 0.01$ and a Zr content of 1.3 at. %. The band gap and film thickness of the samples were determined by spectroscopic ellipsometry to be 4.97 eV and about 220 nm, respectively.

Resistivity and Hall-effect measurements were performed on a 10 × 10 mm^2 sample using the van-der-Pauw method. The electrical conductivity versus T^{-1} is shown in Fig. 7(a). An almost exponential increase in the conductivity with increasing temperature can be observed. For lower temperatures, the measured conductivity deviates from the simple exponential dependence (dashed line) due to the increase in the free carrier mobility. The free carrier concentration is shown in Fig. 7(b) in dependence on the temperature. An overall trend can be observed: the free carrier concentration increases first exponentially and begins to saturate for $T \geq 400$ K. We fitted the dependence using the equations provided in the supplementary material. The respective fits with and without compensation are shown in Fig. 7(b). The results of both the cases are summarized in Table I. Overall, a better agreement between the measured and the fitted data was achieved if compensation was taken into account and yields values for the donor concentration of $N_D = 3 \times 10^{17}$ cm^{-3} with an activation energy of $E_D = 190$ meV. In principle, we expect compensating centers to be present in our heteroepitaxial thin films, but further experiments are required to understand the nature of donors and compensating acceptors as well as the

TABLE I. Results of fits of the temperature-dependent free carrier concentration using equations provided in the supplementary material. N_D and N_A are the concentration of the donor and compensating acceptors, respectively, E_D is the thermal activation energy of the donor, and E_n denotes the difference between the Fermi energy and the energy of the conduction band minimum at room temperature.

Compensation	N_D (cm^{-3})	N_A (cm^{-3})	E_D (meV)	E_n (meV)
Without	3×10^{18}	...	310	370
With	3×10^{17}	4×10^{16}	190	490

electric transport phenomena in κ-Ga_2O_3 in more detail. In comparison to the activation energy of 0.695 eV (without compensation) determined by Pavesi *et al.*[21] between 400 ≤ T ≤ 600 K from conductance measurements on nominally undoped κ-Ga_2O_3 thin films, the donor level investigated here is (independent of the compensation case) significantly closer to the conduction band minimum, demonstrating that it increases n-type conductivity even though E_D is higher than for an effective mass donor. Additionally, from the fits, the difference $E_n = E_c - E_F$ between the conduction band minimum E_c and the Fermi level E_F was calculated for room temperature, which can also be found in Table I. From the resistivity and the Hall-effect measurements, the mobility can be calculated. The plot in dependence on the temperature is shown in Fig. 7(c). For low mobilities (gray shaded area), the error of the measurement becomes rather large and since a lower magnetic field was used for the high temperature measurement, the error is even larger here. From the dependence of the mobility on temperature, we deduced polar-optical scattering[41] to be the dominating scattering mechanism in this temperature range. By fitting of the temperature-dependent mobility, the Debye temperature was estimated to be about 1000 K. The used equation can be found in the supplementary material. Despite the data being well modeled by considering only one scattering mechanism over the measured temperature range,

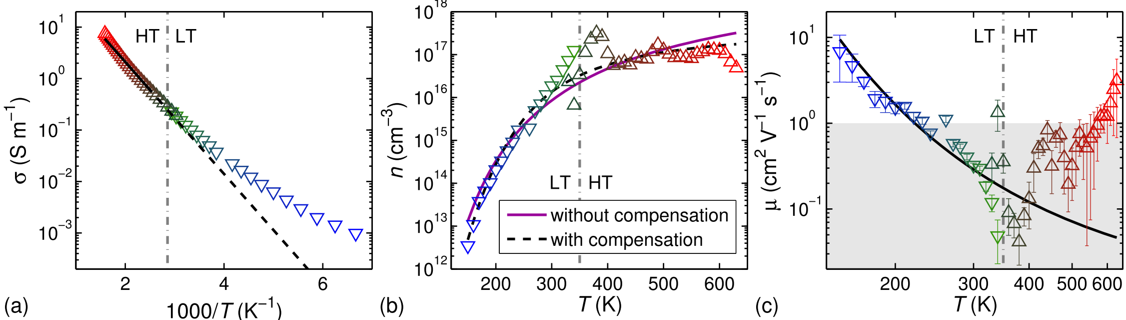

FIG. 7. Results of the temperature dependent resistivity and Hall-effect measurement from low temperatures (labeled LT) to intermediate temperatures and intermediate to high temperatures (labeled HT). (a) shows the conductivity in dependence of T^{-1}. For higher temperatures, the measurements show a linear dependence and for lower temperatures, the measurements deviate from the linear dependence, indicating a more complex behavior. In (b) the free carrier concentration is shown in dependence on the temperature. While the values scatter to some extent due to the noise of the measurement, a clear trend can be seen. The data was fitted with the equation for the cases with and without compensation (see text and Table I for details). (c) shows the mobility in dependence on the temperature. At high temperature, the resulting mobilities are in the range where, especially for the high temperature measurement, the error of the measurement becomes large (gray shaded area). For low temperatures, the mobility may be dominated by polar-optical scattering, as can be seen from the fit of the data.

© Author(s) 2019

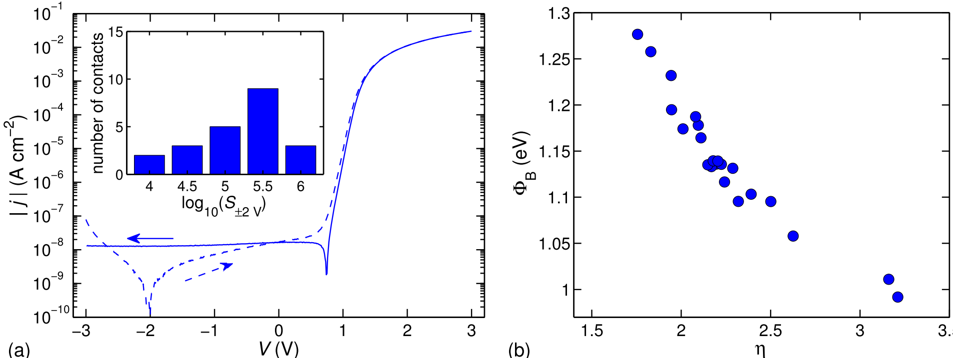

FIG. 8. (a) IV-characteristics of SCs for a bias sweep from negative to positive voltages (dashed lines) and vice versa (solid lines). Instead of the current, the current density j is shown. In the inset, a histogram of the rectification ratios of the rectifying contacts can be found. (b) shows a plot of the effective barrier height vs. the ideality factor determined by fitting the individual characteristics of the rectifying contacts with the thermionic emission model.

it cannot be excluded that other scattering mechanisms also play a role.

In Fig. 8(a), IV characteristics of a representative PtO_δ/κ-$(In,Ga)_2O_3$:Zr Schottky barrier diode is depicted. The plot shows the current density $j = I/A_0$, where A_0 describes the contact area. The first (second) sweep direction is from negative to positive (positive to negative) voltages as indicated by the arrows. The difference between both measurement directions (the position of the zero-crossing) can be explained by a charging current.[42] For the contact shown here, a rectifying behavior is observed and the diode exhibits a low reverse current density of about 1×10^{-8} A cm^{-2}. Overall, 22 contacts were measured and the rectification ratio for V = ±2 V (ratio between the magnitude of the currents measured at these voltages) is depicted as histogram in Fig. 8(a). Some of the contacts exhibit rectification ratios of up to six orders of magnitude. For evaluation of the characteristics, we assumed that the dominating transport mechanism is thermionic emission over the Schottky-barrier, which is reasonable in the mobility and net-doping density range[43,44] discussed above. Since there exists no literature data for the effective mass of κ-Ga_2O_3 and since the ideality factors determined here are too high to evaluate the temperature dependence of the Richardson constant, the effective mass of the free carriers was assumed to be the same as for β-Ga_2O_3 ($m_{\mathrm{eff}} = 0.28m_0$[45,46]). The dependence of Φ_B^{eff} on η is plotted in Fig. 8(b) and shows that with the decreasing ideality factor, the effective barrier height increases almost linearly. A similar behavior was observed by Schmitsdorf *et al.*[47,48] and explained by barrier height inhomogeneities using a patch-like inhomogeneity model developed by Tung.[49] The homogeneous barrier height Φ_B^{hom} was determined by linear extrapolation toward $\eta = 1.02$ to be about 1.35 eV.

In order to further investigate the barrier height inhomogeneities, temperature-dependent IV-measurements between $100 \le T \le 320$ K and $300 \le T \le 700$ K were performed. The associated characteristics are displayed in Fig. 9. For temperatures below 100 K, the series resistance becomes so large that almost no rectification can be observed. For temperatures above 575 K, the needle probes of the Linkam probe stage scratched the surface of the contact due to the thermal expansion and damaged it. The difference in the series resistance between the measurement at low and at high temperatures can be explained by the fact that for the low temperature measurement, an ohmic contact close to the edge of the sample was contacted, while for the high temperature measurement, the ohmic contact that surrounds the measured Schottky contact was used. Furthermore, it can be seen that the series resistance increases strongly with decreasing temperatures. Therefore, the determination of the effective barrier height and the ideality factor becomes difficult at low temperatures, since no exponential region is observed. For temperatures of 200 K and higher, the characteristics were fitted with the model of thermionic emission in order to determine the effective barrier height and the ideality

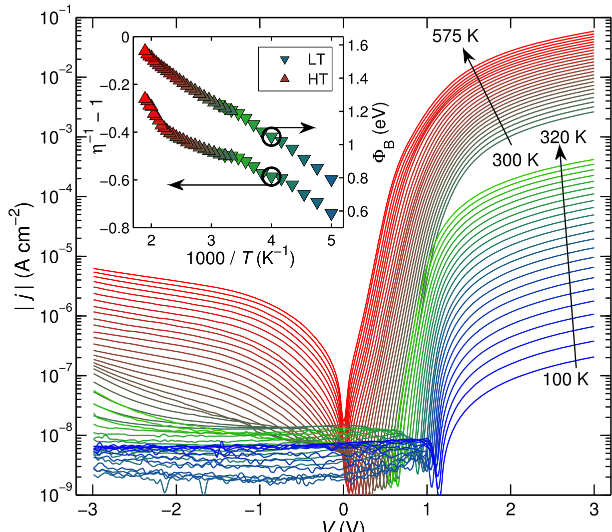

FIG. 9. Temperature-dependent IV-characteristics taken from low temperatures to intermediate temperatures (labeled LT) and intermediate to high temperatures (labeled HT). Here, only the measurement direction going from positive to negative voltages is shown. The higher series resistance in the LT-measurement can be explained by the fact that an ohmic contact on the edge of the sample was used for this measurement. In the inset, the plots of the effective barrier height and $\eta^{-1} - 1$ vs. T^{-1} can be found. Both show an almost linear dependence between 400 K and 200 K.

© Author(s) 2019

factor. According to the theory of Werner and Güttler,[50] a linear dependence of Φ_B^{eff} and $(\eta^{-1} - 1)$ on T^{-1} can be expected if the barrier is laterally inhomogeneous with a Gaussian-shaped barrier distribution. The corresponding plots are shown in the inset of Fig. 9. Both, Φ_B^{eff} and $(\eta^{-1} - 1)$, show a linear dependence on T^{-1} over a large temperature range. At temperatures above 400 K, $(\eta^{-1} - 1)$ deviates from the linear dependence, which might be due to annealing effects. From linear fits in the range between 400 K and 200 K (1000/T = 2.5 and 5 K^{-1}), the mean barrier height and the standard deviation of the barrier distribution as well as their voltage coefficients ϱ_2 and ϱ_3 can be determined to be 1.95 eV, 0.20 eV, 0.13, and −0.02 eV, respectively.

After temperature cycling (highest T = 700 K), a RT IV-measurement was performed on other contacts on the same sample piece. While the ideality factor and the series resistance of the contacts increased and the characteristic became more "rounded," the contacts remained rectifying with rectification ratios up to 5 orders of magnitude. Overall, the rectification ratio decreased by 0.4 orders of magnitude, while the effective barrier height stayed about constant and the ideality factor increased by about 0.2. A plot showing an IV-characteristic before and after the IVT-measurement is provided in the supplementary material.

Because of the high series resistance of the Schottky contacts, investigation by standard capacitance-voltage measurements was not possible. Nevertheless, quasi-static CV measurements can be performed, due to the low reverse current. Exemplary CV-characteristics are shown in the inset of Fig. 10(a). In the main plot of Fig. 10(a), the C^{-2}–V dependency is shown. Different linear regions with different slopes are observed and fitted in order to estimate the net-doping concentration in the corresponding voltage region. The curve in region 1 was linearly extrapolated toward C = 0 in order to estimate the built-in voltage V_{bi}. The results are summarized in Table II.

By numerical modeling, the net-doping density N_t was calculated in dependence on the space charge region width w for each contact on the sample. The mean value of the doping-profile is plotted in Fig. 10(b) with solid lines. The shaded areas correspond to the standard deviations of the measurements on the contact. Note that the change in the net-doping density not necessarily means, that there exists a real change in the doping concentration.[51] It is also possible that at certain voltages, deeper lying defects are lifted above the Fermi energy and hence contribute to the net-doping density for this and lower voltages. This could mean that the minimum observed in the doping-profiles could be due to a deep lying acceptor (also leading to compensation) similar to the case of β-Ga_2O_3 thin films.[42] However, more detailed investigations are necessary to obtain a full understanding. Further, there are differences in the net-doping density determined by QSCV-measurements and the donor concentration determined by Hall-effect measurements, since deeper lying defects contribute to the QSCV-signal. Therefore, the net doping density may differ from fits of the Hall-effect data, especially if materials with a large band gap and high barrier height are investigated.

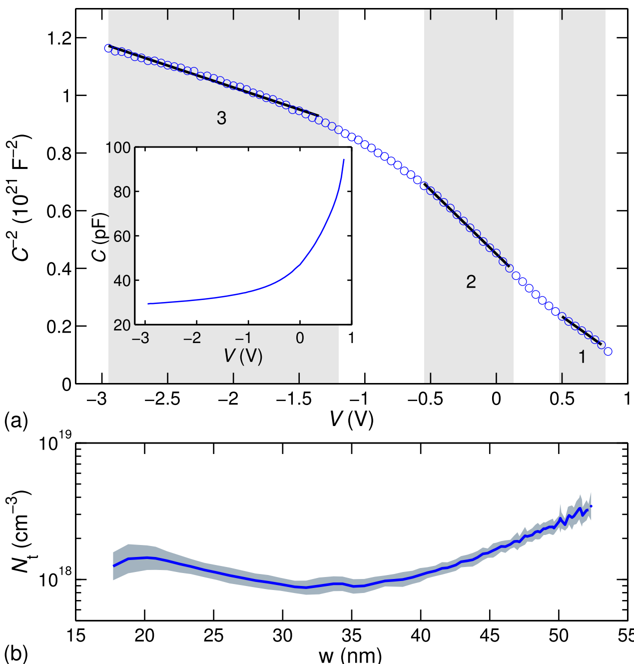

FIG. 10. Results of the quasi-static CV measurement. The inset of (a) shows the capacitance in dependence of the voltage. In (a), C^{-2} vs. V is shown. The differently labeled regions correspond to regions of different linear slope in the plot. The net-doping densities and the built-in potential determined from linear fits can be found in Table II. (b) shows the calculated net-doping profiles. The solid line corresponds to the mean value of measurements on the rectifying contacts and the shaded area to the standard deviation.

In this work we discussed structural, optical, and electrical properties of $(In_xGa_{1-x})_2O_3$ thin films, which were prepared in orthorhombic modification up to x = 0.35 using pulsed-laser deposition. The growth rate of κ-$(In_xGa_{1-x})_2O_3$:Sn is higher than that for monoclinic thin films suggesting that desorption processes were suppressed by the tin-assisted PLD growth. Since Sn is not electrically active in the orthorhombic phase, it is necessary to additionally dope κ-$(In_xGa_{1-x})_2O_3$ to create conducting samples. As a suitable donor, we identified Zr and performed electrical transport measurements on a thin film with an admixture of 1.3 at. % Zr. The donor concentration is about 3×10^{17} cm^{-3} and its thermal activation energy is 190 meV. The rectification ratio of Schottky barrier diodes was as high as six orders of magnitude, and the homogeneous barrier height is 1.35 eV. Temperature-dependent measurements revealed a

TABLE II. Results of the linear fits in the different regions seen in Fig. 10(a). For region 1, also the built-in voltage was determined by linear extrapolation.

N_t (10^{18} cm^{-3})	Region 1	1.3
	Region 2	0.74
	Region 3	1.8
V_{bi} (V)	Region 1	1.20

© Author(s) 2019

strong increase in series resistance with decreasing temperature. Additionally, the DF and pseudo DF were derived for a wide composition range in this work. Overall, the excellent structural and morphological properties of κ-$(In_xGa_{1-x})_2O_3$ compared to β-$(In_xGa_{1-x})_2O_3$ heteroepitaxial thin films make this material interesting for heterostructure-based devices.

See supplementary material for several fitting equations and additional figures about parameters of the Cauchy function and IV-characteristics of a contact at room temperature before and after a temperature dependent IV-measurement to temperatures up to 700 K.

We thank Monika Hahn for PLD target and SC fabrication. We also thank Jörg Lenzner for EDX measurements and Ulrike Teschner for transmission measurements. This work was supported by the European Social Fund within the Young Investigator Group "Oxide Heterostructures" (No. SAB 100310460) and partly by Deutsche Forschungsgemeinschaft in the Framework of Sonderforschungsbereich 762 "Functionality of Oxide Interfaces". A.H. and M.K. acknowledge the Leipzig School for Natural Sciences BuildMoNa. We acknowledge support from Leipzig University within the program of Open Access Publishing.

REFERENCES

[1]Z. Zhang, H. von Wenckstern, and M. Grundmann, IEEE J. Sel. Top. Quantum Electron. **20**, 106–111 (2014).
[2]O. Bierwagen, Semicond. Sci. Technol. **30**, 024001 (2015).
[3]M. Grundmann, H. Frenzel, A. Lajn, M. Lorenz, F. Schein, and H. von Wenckstern, Phys. Status Solidi A **207**, 1437–1449 (2010).
[4]M. Higashiwaki, A. Kuramata, H. Murakami, and Y. Kumagai, J. Phys. D: Appl. Phys. **50**, 333002 (2017).
[5]S. Stepanov, V. Nikolaev, V. Bougrov, and A. Romanov, Rev. Adv. Mater. Sci. **44**, 63–86 (2016).
[6]H. von Wenckstern, Adv. Electron. Mater. **3**, 1600350 (2017).
[7]S. J. Pearton, J. Yang, P. H. Cary, F. Ren, J. Kim, M. J. Tadjer, and M. A. Mastro, Appl. Phys. Rev. **5**, 011301 (2018).
[8]M. Higashiwaki, K. Sasaki, A. Kuramata, T. Masui, and S. Yamakoshi, Appl. Phys. Lett. **100**, 013504 (2012).
[9]S. Fujita, M. Oda, K. Kaneko, and T. Hitora, Jpn. J. Appl. Phys., Part 1 **55**, 1202A3 (2016).
[10]M. B. Maccioni and V. Fiorentini, Appl. Phys. Express **9**, 041102 (2016).
[11]S. B. Cho and R. Mishra, Appl. Phys. Lett. **112**, 162101 (2018).
[12]J. Kim, D. Tahara, Y. Miura, and B. G. Kim, Appl. Phys. Express **11**, 061101 (2018).
[13]I. Cora, F. Mezzadri, F. Boschi, M. Bosi, M. Čaplovičová, G. Calestani, I. Dódony, B. Pécz, and R. Fornari, CrystEngComm **19**, 1509–1516 (2017).
[14]F. Mezzadri, G. Calestani, F. Boschi, D. Delmonte, M. Bosi, and R. Fornari, Inorg. Chem. **55**, 12079–12084 (2016).
[15]Y. Oshima, E. G. Víllora, Y. Matsushita, S. Yamamoto, and K. Shimamura, J. Appl. Phys. **118**, 085301 (2015).
[16]X. Xia, Y. Chen, Q. Feng, H. Liang, P. Tao, M. Xu, and G. Du, Appl. Phys. Lett. **108**, 202103 (2016).
[17]F. Boschi, M. Bosi, T. Berzina, E. Buffagni, C. Ferrari, and R. Fornari, J. Cryst. Growth **443**, 25–30 (2016).
[18]Y. Chen, X. Xia, H. Liang, Q. Abbas, Y. Liu, and G. Du, Cryst. Growth Des. **18**, 1147–1154 (2018).
[19]M. Orita, H. Hiramatsu, H. Ohta, M. Hirano, and H. Hosono, Thin Solid Films **411**, 134–139 (2002).
[20]M. Kracht, A. Karg, J. Schörmann, M. Weinhold, D. Zink, F. Michel, M. Rohnke, M. Schowalter, B. Gerken, A. Rosenauer, P. J. Klar, J. Janek, and M. Eickhoff, Phys. Rev. Appl. **8**, 054002 (2017).
[21]M. Pavesi, F. Fabbri, F. Boschi, G. Piacentini, A. Baraldi, M. Bosi, E. Gombia, A. Parisini, and R. Fornari, Mater. Chem. Phys. **205**, 502–507 (2018).
[22]D. Tahara, H. Nishinaka, S. Morimoto, and M. Yoshimoto, Appl. Phys. Lett. **112**, 152102 (2018).
[23]H. Nishinaka, N. Miyauchi, D. Tahara, S. Morimoto, and M. Yoshimoto, CrystEngComm **20**, 1882–1888 (2018).
[24]H. von Wenckstern, Z. Zhang, F. Schmidt, J. Lenzner, H. Hochmuth, and M. Grundmann, CrystEngComm **15**, 10020 (2013).
[25]S. Müller, H. von Wenckstern, D. Splith, F. Schmidt, and M. Grundmann, Phys. Status Solidi A **211**, 34–39 (2014).
[26]S. Müller, H. Von Wenckstern, F. Schmidt, D. Splith, F. L. Schein, H. Frenzel, and M. Grundmann, Appl. Phys. Express **8**, 121102 (2015).
[27]S. Müller, H. v. Wenckstern, F. Schmidt, D. Splith, H. Frenzel, and M. Grundmann, Semicond. Sci. Technol. **32**, 065013 (2017).
[28]C. Kranert, J. Lenzner, M. Jenderka, M. Lorenz, H. von Wenckstern, R. Schmidt-Grund, and M. Grundmann, J. Appl. Phys. **116**, 013505 (2014).
[29]H. von Wenckstern, D. Splith, A. Werner, S. Müller, M. Lorenz, and M. Grundmann, ACS Comb. Sci. **17**, 710–715 (2015).
[30]H. von Wenckstern, D. Splith, M. Purfürst, Z. Zhang, C. Kranert, S. Müller, M. Lorenz, and M. Grundmann, Semicond. Sci. Technol. **30**, 024005 (2015).
[31]M. Grundmann, Phys. Status Solidi B **248**, 805–824 (2011).
[32]K. Momma and F. Izumi, J. Appl. Crystallogr. **44**, 1272–1276 (2011).
[33]H. Y. Playford, A. C. Hannon, E. R. Barney, and R. I. Walton, Chem. - Eur. J. **19**, 2803–2813 (2013).
[34]C. Sturm, R. Schmidt-Grund, C. Kranert, J. Furthmüller, F. Bechstedt, and M. Grundmann, Phys. Rev. B **94**, 035148 (2016).
[35]H. Fujiwara, *Spectroscopic Ellipsometry: Principles and Applications*, 1st ed. (John Wiley & Sons, 2007).
[36]H. Yao and C. H. Yan, J. Appl. Phys. **85**, 6717 (1999).
[37]C. Tanguy, Phys. Rev. Lett. **75**, 4090–4093 (1995).
[38]C. Tanguy, Phys. Rev. Lett. **76**, 716 (1996).
[39]C. Tanguy, Phys. Rev. B **60**, 10660–10663 (1999).
[40]D. A. G. Bruggeman, Ann. Phys. **416**, 636 (1935).
[41]M. Grundmann, *Transparent Semiconducting Oxides: Materials and Devices*, 1st ed. (Springer, Berlin and New York, 2006).
[42]D. Splith, S. Müller, H. von Wenckstern, and M. Grundmann, Proc. SPIE **10533**, 105330C (2018).
[43]A. Lajn, H. von Wenckstern, M. Grundmann, G. Wagner, P. Barquinha, E. Fortunato, and R. Martins, J. Appl. Phys. **113**, 044511 (2013).
[44]D. Splith, S. Müller, F. Schmidt, H. von Wenckstern, J. J. van Rensburg, W. E. Meyer, and M. Grundmann, Phys. Status Solidi A **211**, 40–47 (2014).
[45]J. B. Varley, J. R. Weber, A. Janotti, and C. G. Van de Walle, Appl. Phys. Lett. **97**, 142106 (2010).
[46]M. Mohamed, C. Janowitz, I. Unger, R. Manzke, Z. Galazka, R. Uecker, R. Fornari, J. R. Weber, J. B. Varley, and C. G. Van de Walle, Appl. Phys. Lett. **97**, 211903 (2010).
[47]R. F. Schmitsdorf, T. U. Kampen, and W. Mnch, J. Vac. Sci. Technol., B: Microelectron. Nanometer Struct.–Process., Meas., Phenom. **15**, 1221–1226 (1997).
[48]R. Schmitsdorf and W. Mönch, Eur. Phys. J. B **7**, 457–466 (1999).
[49]R. T. Tung, Phys. Rev. B **45**, 13509–13523 (1992).
[50]J. H. Werner and H. H. Güttler, J. Appl. Phys. **69**, 1522–1533 (1991).
[51]L. C. Kimerling, J. Appl. Phys. **45**, 1839–1845 (1974).

© Author(s) 2019